Dedong Gao
The State Key Laboratory of Fluid Power
and Mechatronic Systems,
Zhejiang University,
Hangzhou 310027, China;
School of Mechanical Engineering,
Qinghai University,
Xining 810016, China
e-mail: gaodd@zju.edu.cn

Yong Lei[1]
The State Key Laboratory of Fluid Power
and Mechatronic Systems,
Zhejiang University,
Hangzhou 310027, China
e-mail: ylei@zju.edu.cn

Bin Lian
The State Key Laboratory of Fluid Power
and Mechatronic Systems,
Zhejiang University,
Hangzhou 310027, China

Bin Yao
The State Key Laboratory of Fluid Power
and Mechatronic Systems,
Zhejiang University,
Hangzhou 310027, China;
School of Mechanical Engineering,
Purdue University,
West Lafayette, IN 47907
e-mail: byao@zju.edu.cn

Modeling and Simulation of Flexible Needle Insertion Into Soft Tissue Using Modified Local Constraints

Needle insertion is a widely used medical procedure in various minimally invasive surgeries. The estimation of the coupled needle deflection and tissue deformation during the needle insertion procedure is crucial to the success of the surgery. In this work, a novel needle deflection–tissue deformation coupling model is proposed for flexible needle insertion into soft tissue. Based on the assumption that the needle deflection is small comparing to the length of the insertion, the needle–tissue interaction model is developed based on the modified local constraint method, where the interactive forces between the needle and the tissue are balanced through integration of needle–force and tissue–force relationships. A testbed is constructed and the experiments are designed to validate the proposed method using artificial phantom with markers. Based on the experimental analysis, the cutting and friction forces are separated from the force–time curves and used as the inputs into the proposed model. The trajectories of the markers inside the soft tissue are recorded by a CCD camera to compare with the simulation trajectories. The errors between the experimental and simulation trajectories are less than 0.8 mm. The results demonstrate that the proposed method is effective to model the needle insertion procedure. [DOI: 10.1115/1.4034134]

Keywords: needle insertion, needle–tissue interaction, finite-element method

1 Introduction

Needle insertion is a minimally invasive surgical procedure, which uses a slender puncture needle to penetrate into organ or viscera to extract the cells of the organ, or to deliver drugs or treatments to the target areas. It is widely used in biopsy, local anesthesia, brachytherapy, etc. The outcome of the procedure is highly depended on the accuracy of the needle insertion [1]. The main factors influencing the accuracy of the procedure include the limited visibility of the imaging equipments, the uncertainty of the targets, the movement of the surgeon and the patient, and the deformations of needle and soft tissue by their interactions [2]. Among these factors, the deformation of needle and soft tissue affects the needle placement and path planning of the procedure.

In the literature, the needle–tissue interactive forces are the focus of various studies since it is the basis for analyzing the needle deflection and soft tissue deformation. Nienhuys and van der Stappen performed interactive simulations of the needle insertion using the finite-element method (FEM) solved by iterative method and quasi-static stick–slip friction model [3]. A three-dimensional (3D) FEM model of the liver samples was built to model the procedure of needle insertion into soft tissue [4]. Okamura et al. decomposed the needle insertion force into stiffness (a nonlinear spring model), friction (a modified Karnopp model), and cutting forces (a constant for a given tissue) [5]. Moore et al. established an insertion force model for hollow needle insertion into bovine liver [6]. Fukushima et al. obtained a cutting force model using dynamic friction coefficient [7]. Crouch et al. found that the

insertion force is related to velocity in the experiment [8]. Asadian et al. presented the translational friction model developed by the LuGre point friction model, which can be used to refine the beam-based deflection models [9]. The friction forces on needle tip were modeled using the recursive least square method and a disturbance observer in the literature [10]. Barnett et al. investigated the fracture mechanics of porcine skin and developed a physics-based model to explain the dynamic needle–tissue interaction [11].

Studies were conducted on estimating the needle deflection. Misra et al. presented a mechanics-based model for calculating the deflection of the needle, and simulated the needle deflection with FEM [12]. Roesthuis et al. regarded the needle as a cantilever beam and modeled the insertion force for predicting the amount of needle deflection [13]. Sadjadi et al. proposed a fusion approach for needle deflection estimation which was evaluated in brachytherapy procedures on prostate phantoms [14]. The FEM model with triangular plane elements, FEM model with nonlinear beam elements, and the angular spring model were used to calculate the needle deflection, and the results showed that the angular spring model is the simplest and more accurate than the others [15]. The effects of needle geometries, insertion methods, and tissue characteristics on needle–tissue interactive forces were studied experimentally in Refs. [16] and [17].

Soft tissue deformation during needle insertion had also been studied in the literature. Mahvash and Dupont demonstrated that faster needle insertion can produce less tissue deformation and damages [18]. Dimaio and Salcudean proposed a two-dimensional (2D) linear elastostatic material model with FE method, which provided a method for quantifying the needle forces and soft tissue deformations [19]. Pezzementi et al. used a learning algorithm to train a linear 2D mass–spring–damper system, which can approximate tissue deformations [20]. Kobayashi et al. presented

Copyright © 2016 by ASME

a FEM-based liver model, which could accurately reproduce non-linear and viscoelastic responses of displacement at an internally located point with an error below 1 mm [21]. Buijs et al. utilized finite-element method to predict target displacement, in which the organ geometry and boundary conditions surrounding the organ were considered [22].

The needle–tissue coupling models were studied in many literatures. Goksel et al. coupled a quasi-static 3D linear FEM model of the tissue with a flexible needle, which could be used for predicting prostate motion in brachytherapy planning [23]. Haddadi et al. regarded the needle as planar manipulator with angular springs, which related to the needle and soft tissue [24]. In the methods mentioned above, the needle insertion process was considered as a quasi-static process, that is, the insertion result was only decided by the final position. Alterovitz et al. described the coupling of needle and tissue as an iterative process, and built the 2D insertion model considering the effect of the bevel tip and friction [25]. Chentanez et al. presented an efficient method for coupling a 3D finite-element simulation with a 1D inextensible rod with stick–slip friction [26]. In these studies, the nodes of the needle were defined by the tissue's nodes and the transformation of stiffness matrix consumed too much computation time.

As it can be seen from the literature, although various FE models have been developed for the needle insertion procedure, the needle–tissue coupling model remains a challenging task. The reasons are twofold. First, the stiffness matrix of the tissue nodes in many existing studies need to be recomputed in each iterative step because the tissue nodes are used to define the needle nodes with remesh or replacement method, which is not only computational expensive, but also leads to additional simulation errors. Second, since the forces of needle nodes are assigned to the tissue nodes in existing models, the robustness of the iteration is not satisfactory due to the inherent difference between needle stiffness and tissue stiffness. Therefore, a robust and efficient needle–tissue coupling model still needs to be developed so that an interactive needle insertion simulation can be implemented.

The aim of this paper is to develop a novel algorithm for simulating the needle–tissue interactions. The advantage of the proposed algorithm is that the needle–tissue interactive forces are assigned to the nodes of both the needle and soft tissue with modified local constraints, which makes the iterative calculation robust and efficient. The result of this work will enable one to conduct real-time interactive simulation of the needle–tissue procedure, which can be used for virtual training and pre-op needle path planning. The rest of the paper is organized as follows. The models for soft tissue and flexible needle are introduced in Sec. 2. The interactive force analysis during needle insertion into soft tissue is discussed in Sec. 3, followed by the needle–tissue coupling model introduced in Sec. 4. Testbed setup is introduced and comparison between simulation and experimental results are discussed in Sec. 5. Finally, the conclusions and future work are provided.

2 Models for Soft Tissue and Flexible Needle

2.1 Finite-Element Model of Soft Tissue. The focus of this paper is to develop a novel needle–tissue coupling method, hence, we use a linear elastic model to demonstrate the proposed method.
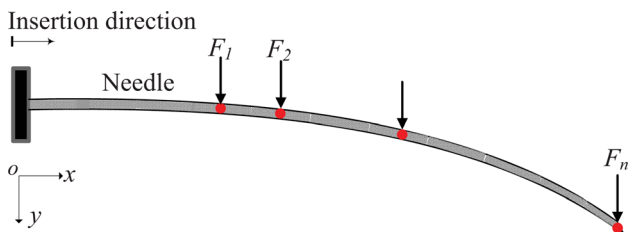

Fig. 1 The cantilever beam model of the needle

Under the assumption of homogeneousity, linear-elasticity, the dynamic behavior of tissue deformation is described as

$$M\ddot{u}(t) + C\dot{u}(t) + Ku(t) = Q(t) \tag{1}$$

where M is the mass matrix, C is the damping matrix, K is the stiffness matrix, Q is the loading matrix, and u denotes the displacement vector of all nodal points.

The Newmark's method is used to integrate the node displacements and velocities over time, as shown in the following equations:

$$\dot{u}_{t+\Delta t} = \dot{u}_t + \left[(1-\delta)\ddot{u}_t + \delta\ddot{u}_{t+\Delta t}\right]\Delta t \tag{2}$$

$$u_{t+\Delta t} = u_t + \dot{u}_t\Delta t + \left[\left(\frac{1}{2}-\xi\right)\ddot{u}_t + \xi\ddot{u}_{t+\Delta t}\right]\Delta t^2 \tag{3}$$

where Δt is the time increment, ξ and δ are the parameters of Newmark's method which decide the accuracy and the stability. Substituting Eqs. (2) and (3) into Eq. (1), the displacement $u_{t+\Delta t}$ at time $t + \Delta t$ is calculated as

$$
\begin{aligned}
&\left(K + \frac{1}{\xi\Delta t^2}M + \frac{1}{\xi\Delta t}C\right)u_{t+\Delta t} = Q_{t+\Delta t} \\
&+ M\left[\frac{1}{\xi\Delta t^2}u_t + \frac{1}{\xi\Delta t}\dot{u}_t + \left(\frac{1}{2\xi}-1\right)\ddot{u}_t\right] \\
&+ C\left[\frac{\delta}{\xi\Delta t}u_t + \left(\frac{\delta}{\xi}-1\right)\dot{u}_t + \left(\frac{\delta}{2\xi}-1\right)\Delta t\ddot{u}_t\right]
\end{aligned} \tag{4}
$$

where $Q_{t+\Delta t}$ is the load at time $t + \Delta t$, and u_t, $\dot{u}_t$, and $\ddot{u}_t$ are the displacement, velocity, and acceleration, respectively. When $\delta \geq 0.5$ and $\xi \geq 025(0.5 + \delta)^2$, the algorithm is unconditionally stable. In this work, all the simulations were based on $\delta = 0.5$ and $\xi = 0.25$.

Equation (4) can be expressed with the general force and displacement. After dividing the element mesh and defining the material properties, the relationship between the general force and displacement of the tissue nodes can be written as

$$\mathbf{K}_{\text{tissue}} \cdot u = F \tag{5}$$

where F and u are the general force and displacement vectors of all nodal points, respectively, and $\mathbf{K}_{\text{tissue}}$ is the general stiffness matrix of soft tissue.

2.2 Flexural-Cantilever Model of Flexible Needle. Although many needles consist of a stylet and a hollow cannula, in this work the flexible needles are simplified as a solid bar. The length of the flexible needle is assumed as a constant. Hence, the needle can be regard as a cantilever, as shown in Fig. 1. In the figure, the acted forces on the nodes (the solid points 1, 2, ..., n) are $F_y = [F_1, F_2, ..., F_n]^{\text{T}}$, and the corresponding deflections along the y direction are $\omega = [\omega_1, \omega_2, ..., \omega_n]^{\text{T}}$. The relationship between the deflection ω and the force F_y is shown in the following equation:

$$
\begin{cases}
\omega_1 = k_1\left(\sum\limits_{i=1}^{i=n}F_i\right) \\
\omega_2 = k_2\left(\sum\limits_{i=2}^{i=n}F_i\right) + \Delta_{1,2} \times \dfrac{3k_1}{2l_1}\left(\sum\limits_{i=1}^{i=n}F_i\right) \\
\quad\quad\quad\quad\quad\vdots \\
\omega_n = k_nF_n + \sum\limits_{j=1}^{j=n-1}\left(\Delta_{j,n} \times \dfrac{3k_j}{2l_j}\left(\sum\limits_{i=j}^{i=n}F_i\right)\right)
\end{cases} \tag{6}
$$

where $k_i = \left(l_i^3/3\text{EI}\right)$, $\Delta_{i,j}$ denotes the distance between point i and point j, and l_i denotes the distance between point j and the
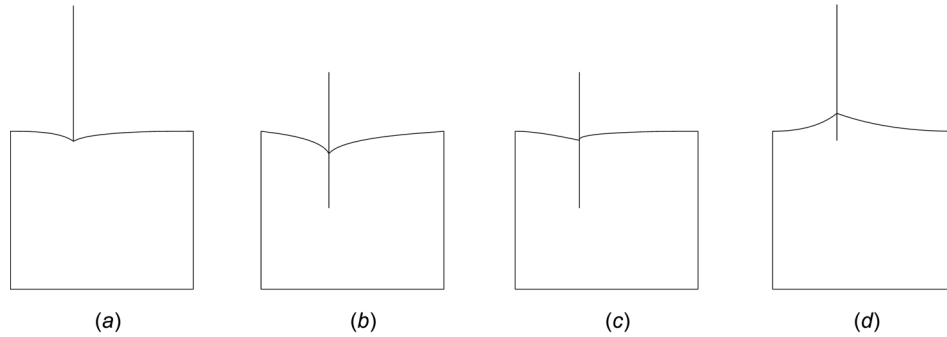
Fig. 2 The four processes of the needle insertion. (*a*) Process 1, the needle touches the surface of tissue and does not penetrate into the tissue. (*b*) Process 2, the needle penetrates into the tissue at a certain depth. (*c*) Process 3, the needle holds its position relative to the tissue. (*d*) Process 4, the needle is retreated from the tissue.

supporting point. Since ω is a linear function of F in Eq. (6), it can be rewritten as shown in the equation given below

$$F_y = \bar{\mathbf{K}} \cdot \omega \qquad (7)$$

where $\bar{\mathbf{K}}$ is a $n \times n$ matrix.

The force F_i acted on the tip node is decomposed into two components: the radial F_{ix} and axial F_{iy} forces. Under the assumption of small deformation, F_{ix} is far less than F_{iy}, and F_{ix} is approximated as zero. Define $F = [F_{1x}, F_{1y}, \ldots, F_{nx}, F_{ny}]^{\mathrm{T}} (F_{ix} = 0, F_{iy} = F_i)$ and $u = [u_{1x}, u_{1y}, \ldots, u_{nx}, u_{ny}]^{\mathrm{T}} = [u_{1x}, \omega_1, \ldots, u_{nx}, \omega_n]^{\mathrm{T}}$ in the plane coordinates xoy. Then, Eq. (7) can be rewritten as

$$F = \begin{bmatrix} 0 & 0 & 0 & \cdots & 0 \\ 0 & K_{1,1} & 0 & \cdots & K_{1,n} \\ 0 & 0 & 0 & \cdots & 0 \\ \vdots & \vdots & \vdots & \ddots & \vdots \\ 0 & K_{n,1} & 0 & \cdots & K_{n,n} \end{bmatrix}_{2n \times 2n} \cdot u = \hat{\mathbf{K}}_n \cdot u \qquad (8)$$

where $\hat{\mathbf{K}}_n$ is a $2n \times 2n$ matrix, which is the stiffness matrix of the needle, F_{ix} are the forces acted on node i, and u_{ix} are the displacements of node i in the x direction.

In Eq. (8), the stiffness matrix contains a lot of zero rows and columns, which means that the force and displacement of needle nodes in the y direction can be balanced only. Since the needle can move freely, there are no constraints for the displacements u_{ix} in the x direction. The constraints in the x direction are the friction and cutting forces, which is reflected in the model of soft tissue.
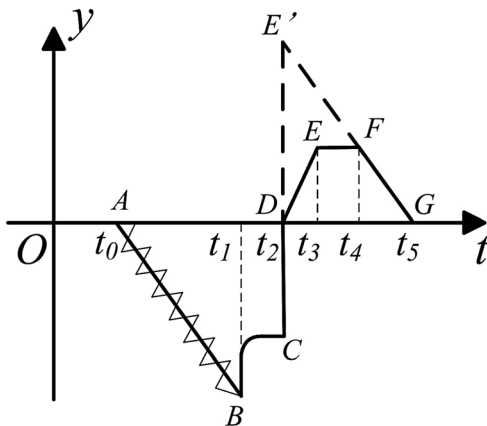
3 Force Analysis of Needle–Tissue Interaction

The procedure of flexible needle insertion into soft tissue is taken as four different processes, as shown in Fig. 2. In process 1, the needle touches the surface of tissue, but doesn't penetrate into the tissue. The needle tip is loaded by the stiffness force of soft tissue. In process 2, the needle penetrates into the tissue at a certain depth. The displacement of the needle is constrained, and the tissue is constrained by the surroundings. In process 3, the needle reaches the target and keeps its position relative to the tissue. The strain energy is released in this process, and the needle is constrained by the force of the tissue. In process 4, the needle is retreated from the tissue, and only the friction force affects the needle.

According to the experimental studies, typical force–time curves for the homogeneous and inhomogeneous materials are shown in Fig. 3. In this figure, the needle contacts to the tissue's surface at t_0 and moves into the tissue at a constant velocity from t_0 to t_1. The dynamic friction and cutting forces affects the insertion procedure between t_0 and t_1, and the cutting force decreases to zero at t_2. The needle stops at t_1, and it keeps its position in the tissue from t_1 to t_2. The needle pulls out from the tissue with friction between t_2 and t_5. In the figure, the line AB denotes that the needle is acted by the friction force and periodic cutting force. The line segment $DEFG$ denotes the force–time curve of the inhomogeneous tissue material, and $DE'FG$ is the force–time curve of the homogeneous material tissue. The slopes of segment DE and segment FG are different for the difference of the static friction coefficient and dynamic friction coefficient. We will model the forces of needle insertion as the following.

Let us first assume the needle in process 1 is normal to the surface of the tissue, that is, the needle contacts to the tissue surface at a point, but does not have it punctured, as shown in Fig. 2(*a*). Considering the constraints of the contact points and the boundary, the radial force F_{iy} is proportional to the needle deflection [27]. Hence, the radial direction of the contact point can be modeled with a spring model, as shown in Fig. 4, where K_1 is the elastic coefficient of the needle. K_2 denotes the proportional coefficient between the radial force by the tissue and the deflection, which can be determined by the experimentation.

Fig. 3 Illustration of typical force–time curves of needle insertion
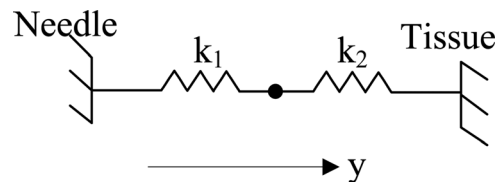

Fig. 4 The spring model in radial direction. The point in the middle denotes the contact point of tissue and needle.

When the needle contacted the surface vertically, the interactive relationship between the needle and the tissue is divided into three states, as shown Fig. 5. At the beginning of needle insertion, the needle tip contacts the surface of soft tissue and only the tissue deformation happens, when the needle is at state 1. When the needle is bent by the tissue's squeeze force, the needle is at state 2. With the increase of needle deflection, the tissue node' force is balanced by the radial force of the needle tip, and the needle is at state 3. The equilibrium state (state 3) can be calculated by the two known states (state 1 and 2). The specific steps are as follows: (a) at the state 1, the needle does not bend, and the axial displacement and the radial force F_1 of the contact nodal point are solved by the FE equation Eq. (5). (b) At the state 2, the radial force F_1 and the deflection are added to the needle's node, and the radial force F_2 is updated for the state 2. (c) The needle and the tissue are at equilibrium at state 3. The needle deflection at state 3 can be solved using the corresponding spring model.

From Fig. 5, the radial forces F_1 and F_2 in state 1 and 2 can be determined by the following equations, respectively,

$$\begin{cases} F_1 = F_{\text{tissue1}} \\ y_1 = 0 \end{cases} \tag{9}$$

$$\begin{cases} F_2 = F_{\text{tissue2}} - F_1 \\ y_2 = \dfrac{F_1}{K_1} \end{cases} \tag{10}$$

When the needle and the tissue are at equilibrium, the needle deflection can be solved as shown in the following equation from the spring model;

$$\begin{cases} F_3 = 0 \\ y_3 = y_1 - F_1 \dfrac{y_2 - y_1}{F_2 - F_1} = -\dfrac{F_1^2}{(F_2 - F1)K_1} \end{cases} \tag{11}$$

where F_j and y_j are the force and the needle's deflection at the state j ($j = 1, 2, 3$). F_{tissue1} and F_{tissue2} are the forces at contact point at state 1 and state 2, respectively.

When the needle is not normal to the surface of the tissue, the coordination systems of needle–tissue interaction will be created, as shown in Fig. 6, where XOY and xoy are the frames of the soft tissue and the flexible needle, respectively. The inclination angle θ is defined as the angle between the needle's axial direction and vertical direction. The transformation from the frame xoy to the frame XOY is described as given in the below equation

$$\begin{bmatrix} X \\ Y \end{bmatrix} = \begin{bmatrix} \cos(\pi/2 + \theta) & -\sin(\pi/2 + \theta) \\ \sin(\pi/2 + \theta) & \cos(\pi/2 + \theta) \end{bmatrix} \begin{bmatrix} x \\ y \end{bmatrix} = R_e \begin{bmatrix} x \\ y \end{bmatrix} \tag{12}$$

where R_e is the transformation matrix, and $[x, y]^{\text{T}}$ and $[X, Y]^{\text{T}}$ are the vectors in xoy and XOY, respectively. The force and displacement vectors are transformed between xoy and XOY with Eq. (12). The origin points of xoy and XOY are fixed at the tail of flexible needle. The x-axis is along the original needle's direction, and the y-axis is normal to the x-axis which direction is pointed at the deflection direction. The dashed line represents x-axis (the undeflected needle), and the horizontal dashed line represents the undeformed surface of soft tissue. ω denotes the radial displacement of the needle tip.

Since the flexible needle is modeled as a cantilever beam, the relationship of the needle deflection and the penetration depth is shown in the equation given below

$$\omega = \cot\theta(x - x_0), \tag{13}$$

where x is the abscissa of the contact point, and x_0 denotes its abscissa with respect to the needle undeformed.
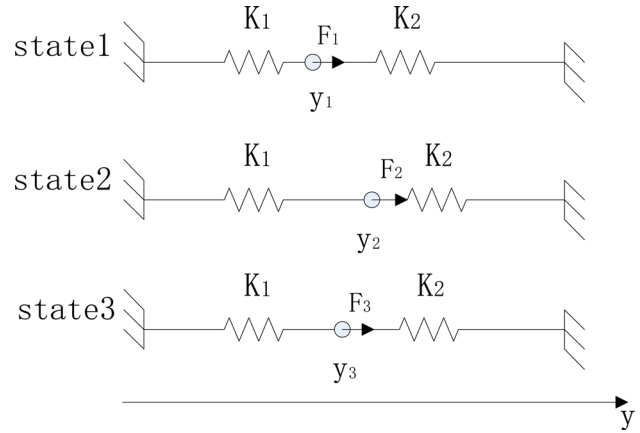
Fig. 5 The relationship between force and displacement in different state

For the linear-elastic model, i.e., $\omega = (\omega_0/x_0)x$. Hence, the needle deflection ω and the insertion depth x are derived from the equation given below

$$\begin{cases} \omega = \dfrac{\omega_0 x_0 \cot\theta}{x_0 \cot\theta - \omega_0} \\ x = \dfrac{x_0^2 \cot\theta}{x_0 \cot\theta - \omega_0} \end{cases} \tag{14}$$

where ω_0 denotes the needle deflection when the insertion depth is x_0, and θ is the inclination angle of the needle tail's tangent line and the surface's normal line.

The force acted on the tip can be approximated with the reaction force of the tissue nodal point which contacts to the tip. The forces of tissue's node is calculable with Eq. (5).

For the processes other than process 1, according to the typical force–time curve obtained from experiments, as shown in Fig. 3, the axial force is a combination of the friction and cutting forces, while the friction force is proportional to the displacement of the needle, and the cutting force is regarded as a constant, details of the experiments will be introduced in Sec. 5.1.

4 Needle–Tissue Coupling Model

In this paper, a new needle–tissue coupling modeling method is developed to couple the needle–tissue interactions, in which the interactive forces are balanced through needle–force relationship and tissue–force relationship. In this section, the coupling model will be first introduced at the special condition, i.e., when the
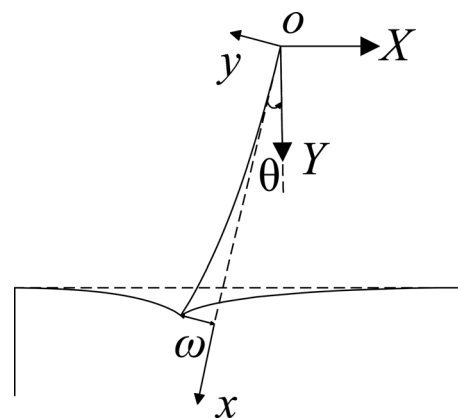

Fig. 6 The schematic diagram of positional relationship between needle and tissue's surface

needle nodal points coincide with the tissue nodal points. Then, the model at the general condition is introduced for the situation that the needle nodal points does not coincide with the tissue nodal points, and the needle track is defined to couple the nodes of both the needle and the tissue. Please notice that although the homogeneous linear-elastic material model is used when introducing the needle–tissue coupling model, this model can also be applied on the inhomogeneous tissues. Because the principal idea of the proposed method is that the forces acting on the needle are distributed to soft tissue, and the forces are transmitted inside the nodes of soft tissue, which can be modeled with homogeneous or inhomogeneous properties. Details of the proposed method is as follows.

4.1 Coupling Model at the Special Condition. The special condition includes two scenarios. The first scenario is at the beginning of needle insertion, where the tissue nodal nodes on the tissue surface are chosen as the contact nodal points with the needle. In this case, the tissue has small deformation, and the nodes of needle coincide with that of the soft tissue. The second scenario occurs during the insertion procedure, where the needle nodal points are very close to the tissue nodal points.

When the needle nodal points coincide with the tissue node points, the forces and reactive forces at the needle and tissue node points are counteracted. Using Eqs. (8) and (12), the force and displacement of needle in tissue coordination can be rewritten as shown in the equation given below

$$\begin{cases} F = K_{\text{needle}} \cdot u \\ F = R \cdot F_G \\ u = R \cdot u_G \end{cases} \Rightarrow \begin{cases} F_G = R^{-1} \cdot K \cdot R \cdot u_G \\ R = \text{Diag}\left(\underbrace{R_e^{\text{T}}, R_e^{\text{T}}, \ldots, R_e^{\text{T}}}_{n}\right) \end{cases} \quad (15)$$

where R is a diagonal matrix combined with R_e, F_G, and u_G are the force and displacement vectors of the needle in the tissue frame XOY in Fig. 6, respectively.

Let us define $\mathbf{K}_{\text{needle}} = R^{-1}KR$, Eq. (15) can be derived as

$$F_G = \mathbf{K}_{\text{needle}} \cdot u_G \quad (16)$$

where $\mathbf{K}_{\text{needle}}$ denotes the stiffness matrix of flexible needle in the tissue frame XOY.

The needle insertion cause the change of the stiffness of the whole system, as shown in Fig. 7, in which the nodes in the shadow area are strengthened by the coupling of needle and tissue. The nodes marked as Δ are the combinations of nodes of tissue
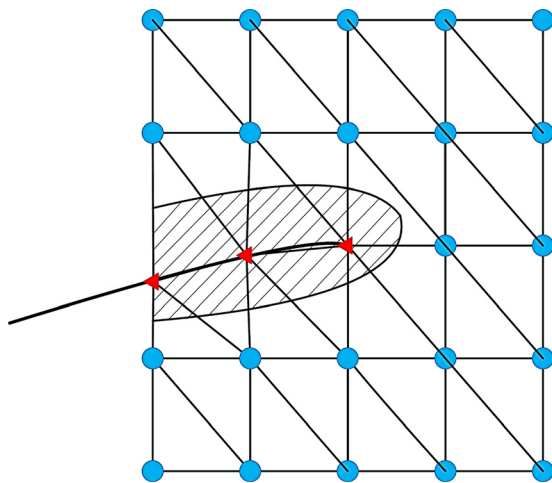

Fig. 7 Diagram for the strengthened stiffness of needle and tissue, "Δ" denotes the needle node point and "○" denotes the tissue node point

and needle. Hence, the stiffness of the strengthened nodes can be unified into the tissue frame XOY, and it is calculated as $\mathbf{K}_G = \mathbf{K}_{\text{tissue}} + \mathbf{K}_{\text{needle}}$. Combining Eq. (16) with Eq. (5), the needle–tissue coupling model is calculated as in the following equation:

$$\mathbf{K}_G \cdot u = \mathbf{F} \quad (17)$$

4.2 Coupling Model at the General Condition. When the needle node points do not coincided with tissue node points, the relationship of needle and tissue are built by the needle track. The needle track is unique for each insertion process, and the needle coincides with the track. Therefore, the needle node points are defined by tissue node points nearby, as shown in Fig. 8.

Let us take point P_1, for example. Because the relative position among point P_1, $S1_1$, and $S2_1$ is unchanged, the position of the intersection point P_1 can be decided by the point $S1_1$ and point $S2_1$, as shown in the equation given below

$$u_{P_1} = \lambda u_{S2_1} + (1 - \lambda)u_{S1_1} \quad (18)$$

where u_{P_1} denotes the coordinate of point P_1 and $\lambda = \left(l_{P_1 S1_1}/l_{S1_1 S2_1}\right)$. According to Fig. 8, the relationship of the deflections at nodal point P_i is written as

$$\begin{bmatrix} \omega_{P_1} \\ \omega_{P_2} \\ \omega_{P_3} \\ \omega_{P_4} \\ \omega_{P_5} \\ \omega_{P_6} \end{bmatrix} = \begin{bmatrix} (1 - \lambda_1)\omega_{S1_1} + \lambda_1\omega_{S2_1} \\ (1 - \lambda_2)\omega_{S1_2} + \lambda_2\omega_{S2_1} \\ (1 - \lambda_3)\omega_{S1_2} + \lambda_3\omega_{S2_2} \\ (1 - \lambda_4)\omega_{S1_3} + \lambda_4\omega_{S2_2} \\ (1 - \lambda_5)\omega_{S1_3} + \lambda_5\omega_{S2_3} \\ (1 - \lambda_6)\omega_{S1_4} + \lambda_6\omega_{S2_3} \end{bmatrix} = K_{S \text{ to } P} \begin{bmatrix} \omega_{S1_1} \\ \omega_{S1_2} \\ \omega_{S1_3} \\ \omega_{S1_4} \\ \omega_{S2_1} \\ \omega_{S2_2} \\ \omega_{S2_3} \end{bmatrix} \quad (19)$$

where ω_i denotes the deflection of point i, and λ_i denotes the coefficients of points P_i in the needle frame. For the whole needle–tissue interaction, $K_{S \text{ to } P}$ is a $N \times M$ matrix, $N = 2n$ is the number of intersected points, and M is the number of tissue nodes whose elements are pierced by the needle. If the nodes of the needle are very close to the tissue nodes, the calculation can be approximated as the special condition.

Different from needle's position, the forces on the needle node are determined by the relationship between elements of the needle and the tissue. Since the sizes of elements of the needle and the tissue are changeable during the simulation, without loss of generality, we assume that the size of element does not change significantly between each simulation iteration, hence, the force can be allocated by the state in Fig. 5.

In each iterative step, the soft tissue is considered in static situation. Take the segment $S1_1 S2_1$ in Fig. 8, for example, the point P_1 is the intersected point of $S1_1 S2_1$ and the needle. The segment in iterate step can be considered as a cantilever, so the force on the point P_1 is assigned to the points $S1_1$ and $S2_1$, as shown in the equation given below
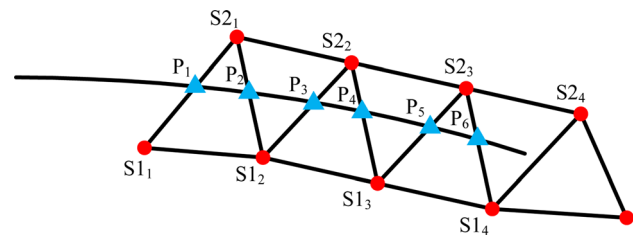

Fig. 8 Schematic plot of track. Δ denotes the needle nodes, they are also the intersected points of the needle and tissue elements. "●" denotes the tissue nodes who is near the needle.

$$\begin{bmatrix} F_{S1_1} \\ F_{S2_1} \end{bmatrix} = \begin{bmatrix} (1-\lambda_1)F_{P_1} \\ \lambda_1 F_{P_1} + \lambda_2 F_{P_2} \end{bmatrix} \tag{20}$$

Under the assumption above, the relationship of the forces on the nodes of the needle and soft tissue is shown as the following equation:

$$\begin{bmatrix} F_{S1_1} \\ F_{S1_2} \\ F_{S1_3} \\ F_{S1_4} \\ F_{S2_1} \\ F_{S2_2} \\ F_{S2_3} \end{bmatrix} = \begin{bmatrix} (1-\lambda_1)F_{P_1} \\ (1-\lambda_2)F_{P_2} + (1-\lambda_3)F_{P_3} \\ (1-\lambda_4)F_{P_4} + (1-\lambda_5)F_{P_5} \\ (1-\lambda_6)F_{P_6} \\ \lambda_1 F_{P_1} + \lambda_2 F_{P_2} \\ \lambda_3 F_{P_3} + \lambda_4 F_{P_4} \\ \lambda_5 F_{P_5} + \lambda_6 F_{P_6} \end{bmatrix} = K_{P \text{ to } S} \begin{bmatrix} F_{P_1} \\ F_{P_2} \\ F_{P_3} \\ F_{P_4} \\ F_{P_5} \\ F_{P_6} \end{bmatrix} \tag{21}$$

where F_i denotes the force of point i in radial direction, $K_{P\text{to}S}$ is a $M \times N$ matrix. For the needle–tissue coupling model at general condition, the coupling stiffness matrix $\hat{\mathbf{K}}_G$ is calculated as shown in the equation given below

$$\hat{\mathbf{K}}_G = K_{P\text{to}S} \cdot \hat{\mathbf{K}}_n \cdot K_{S\text{to}P}, \tag{22}$$

$\mathbf{K}_G$ and $\hat{\mathbf{K}}_G$ are the coupling stiffness matrices at the special and general conditions, respectively.

4.3 Solution to Needle–Tissue Coupling Model.
According to the coupling model above, the general process of needle insertion is shown in Fig. 9, where $P = \{P_1, \ldots, P_7\}$ denotes a set of tissue nodes around the needle. $B = \{B_1, \ldots, B_9\}$ denotes a set including the boundary nodes, which are fixed.

Substituted Eq. (22) into Eq. (17), the general model for needle–tissue coupling model can be described as

$$\hat{\mathbf{K}}_G \cdot \begin{bmatrix} u_P \\ u_R \\ u_B \end{bmatrix} = \begin{bmatrix} K_{11} & K_{12} & K_{13} \\ K_{21} & K_{22} & K_{23} \\ K_{31} & K_{32} & K_{33} \end{bmatrix} \cdot \begin{bmatrix} u_P \\ u_R \\ u_B \end{bmatrix} = \begin{bmatrix} F_P \\ F_R \\ F_B \end{bmatrix} \tag{23}$$

where the subscript $(\cdot)_P$ denotes the tissue notes near the needle, subscript $(\cdot)_B$ denotes the fixed notes or the boundary notes, and subscript $(\cdot)_R$ denotes the other points. F_P and u_P are the forces and displacements of nodes in the set P, F_B, and u_B are the forces and displacements of nodes in the set B, F_R, and u_R are the forces and displacements of other nodes inside the tissue.
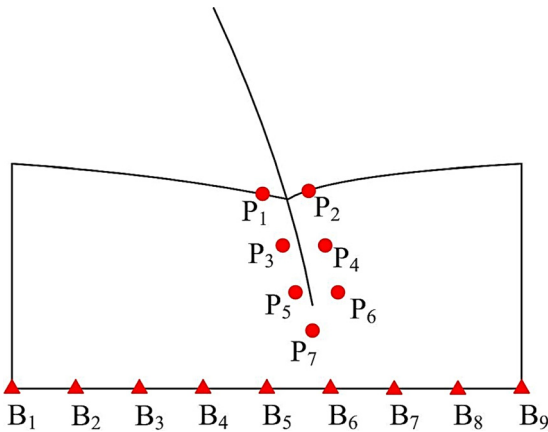

Fig. 9 General process of needle insertion, "○" denotes the tissue node whose element is pierced by the needle, "△" denotes the tissue node whose element is fixed

In the procedure of needle insertion into soft tissue, the fixed nodes has no displacements, i.e., $u_B = 0$. The nodes inside the tissue do not affect by the external forces, i.e., $F_R = 0$. F_P can be solved with Eq. (19). Therefore, the solution to the equation is described as shown in the following equation:

$$\begin{bmatrix} u_P \\ u_R \end{bmatrix} = \begin{bmatrix} K_{11} K_{12} \\ K_{21} K_{22} \end{bmatrix}^{-1} \begin{bmatrix} F_P \\ 0 \end{bmatrix} \tag{24}$$

4.4 Implementation of the Simulation Algorithm.
In order to simulate the needle–tissue interactive procedure, the algorithm is divided into three parts: preprocessing, interactive calculation, and postprocessing. In the preprocessing, the position of the tip is assigned, the nodal points of needle track is defined according to Fig. 8, and the tissue model is meshed. In the interactive calculation procedure, the cutting and friction forces are loaded on the tissue model with Eq. (19), and the effective coupling stiffness matrix is generated and updated with Eq. (17). Then, the forces are transformed into the loads on the nodes of needle–tissue FE model, and the solution is obtained with Eq. (24). The solved displacements of needle and tissue nodal points are used for determining the process of needle insertion. The procedure of the calculation is illustrated as Fig. 10, and it was implemented in MATLAB. The iteration time for a 1061×1061 2D grid mesh is 10 ms on an Intel i7-3.5 GHz dual-core machine running Linux OS.

5 Experimentations and Simulation

Experiments are designed to validate the simulation results. Polyvinyl alcohol hydrogel (PVA-H) based phantom is used to emulate the soft tissue, for which the markers inside the tissue are
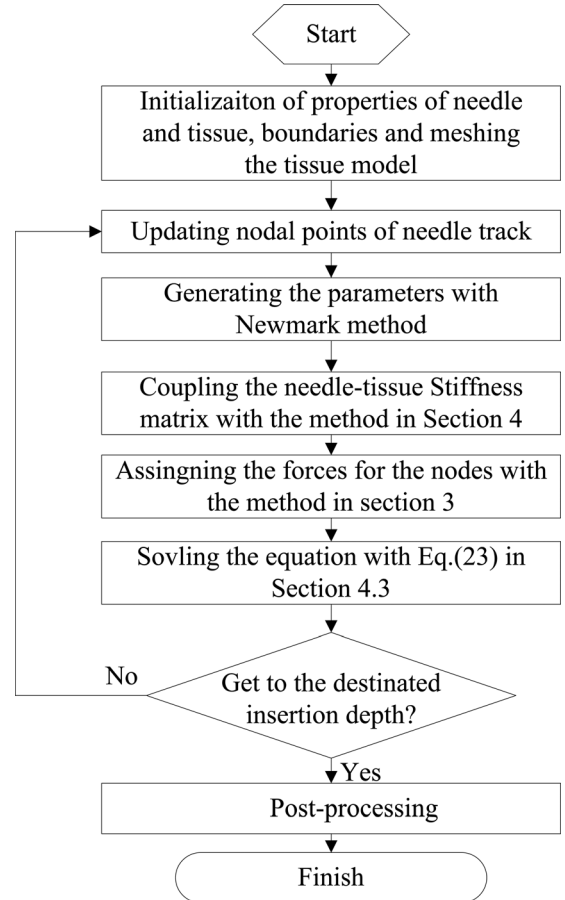

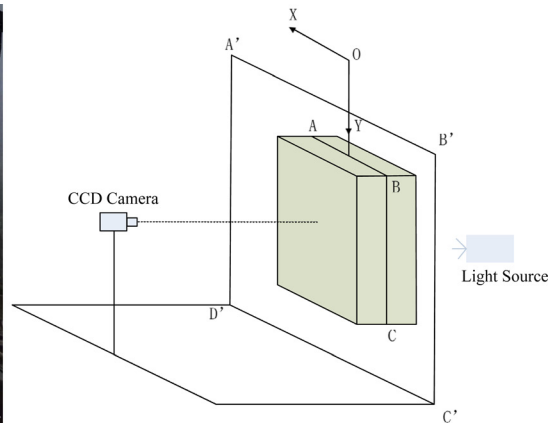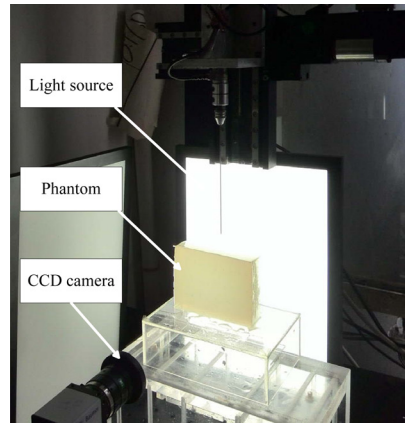Fig. 10 Algorithm of needle–tissue interactive simulation

Fig. 11 Experimental setup for needle insertion, including two translational stages, a CCD camera, a force/torque sensor, a PVA-H phantom, a percutaneous transhepatic cholangiogram needle, and a light-emitting diode light source. Left: experimental setup. Right: diagram for imaging acquisition.

recorded using the CCD camera. The experimental and simulation results are compared using the displacements of the markers.

5.1 Experimental Setup. The experimental setup is designed as Fig. 11. It includes two translational stages, a CCD camera, a force/torque sensor, a PVA-H phantom, a percutaneous transhepatic cholangiogram needle, and a light-emitting diode light source. In the experiments, the 13 cm-long percutaneous transhepatic cholangiogram needles with bevel tip are inserted into the PVA-H phantom. The needle is steered to insert into soft tissue with two 2-degree-of-freedom translational stages. The force data are acquired with a force/torque sensor from ATI Industrial Automation, Apex, NC. The needle moves in the plane $A'B'C'D'$, in which the markers (small beads embedded inside the phantom) are located. For ensuring the homogeneous light on the phantoms, the light-emitting diode light source is normal to $A'B'C'D'$.

PVA is a widely used biocompatible synthetic polymer material in various biomedical field. The PVA-H phantoms used in this work are made of dimethyl sulfoxide (50%) and polyvinyl alcohol (8%). The Young's modulus of the phantom lies between 10 KPa and 50 KPa, which is similar to human liver, whose modulus is 10–70 KPa. The Poisson ratio of the phantom is 0.49. Although the real tissue/organ shows inhomogeneousity and nonlinearity properties, which cannot be reflected by the phantom used in this work, the PVA-H phantom has two advantages: first, it has good linear-elasticity property, which is ideal for validating the tissue/needle deformation model, second, it has good transparency, which makes it easy to record the trajectories of the markers inside the phantom.

Two experimentations are designed to validate the cantilever model of the needle and the force model in Fig. 3. First, the
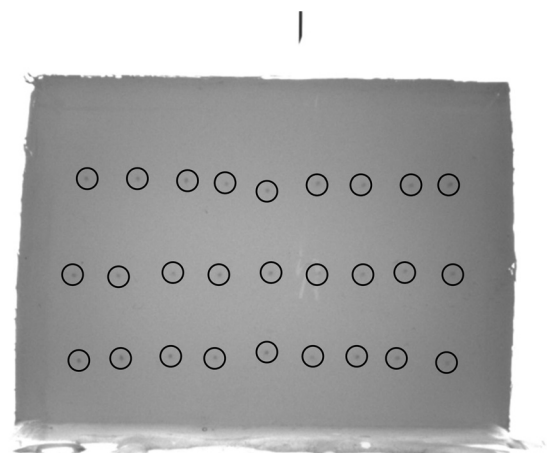

Fig. 13 Locations of the markers inside the phantom

different PVA-H phantoms are made for testing the properties of PVA-H phantom, and the needle is inserted into the same position of the phantom six times in each trial, the results shown in Fig. 12. The experimental results show that the force–time curves in Fig. 12 agree with those of the model in Fig. 3, and the friction and cutting forces have good repeatability and linearity. From Fig. 12, the friction along the needle is steady increased, and the friction coefficients of the insertion process is approximate with those of retreat process. The friction coefficients for different PVA-H phantoms can be calculated with the force–time curves in Fig. 12.

Additional experiments are conducted to determine the proportional coefficients K_2 between the radial force and the needle deflection. In the experiments, the movement of the needle tip is captured by the CCD camera, and the forces in the radial direction
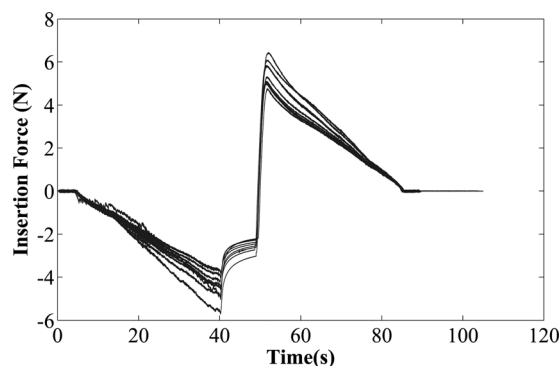

Fig. 12 Force–time curves for six different PVA-H phantoms when insertion at the same position

Table 1 The parameters in the simulation

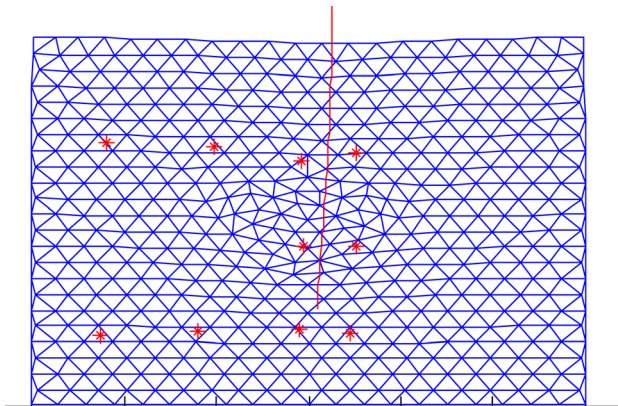| Parameter	Value
Tissue's dimension	$120 \times 80 \ \mathrm{mm}^2$
Tissue's Young's modulus	15 KPa
Needle's Young's modulus	2.1 GPa
Tissue's Poisson ratio	0.49
Areal density	$24 \ \mathrm{kg/m}^2$
The coordinate of contact point	[0, 0] mm
The tip's angle	20 deg
Needle's moment of inertia	$0.7854 \ \mathrm{mm}^4$
Insertion speed	3 mm/s

Fig. 14 A snapshot of the simulation output, and "＊" points are the targets
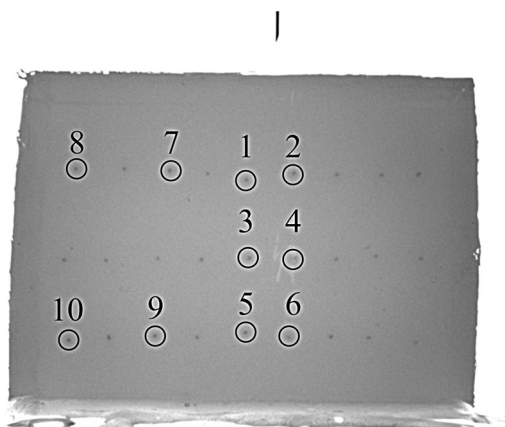

Fig. 15 Picture of the phantom with markers embedded

are collected by the force sensor. Then, the proportional coefficients K_2 can be obtained by the radial displacements of needle tip and the forces in the radial direction using the least square regression method.

To monitor the deformation inside the phantom, three rows of the markers (small beads placed inside the phantom) are planted inside the phantom, and the distance between the two beads is 1 cm, as shown in Fig. 13. The markers at top row can illustrate the displacements of tissue nodes that approach the surface. The displacements of the nodes inside the tissue are investigated by

the markers of middle row. The markers at bottom row illustrate the tissue nodes nearby the boundary.

At the beginning of each experiment, the needle is placed above the phantom surface at 1 cm. The procedure of needle insertion into the phantom includes three processes: inserting into the phantom, stoping at the insertion depth of 6 cm, and then retreating from the phantom. The insertion and retreat are carried out with a constant velocity at 3 mm/s. Fifty four images are captured during each needle insertion procedure, from which the trajectories of all the markers are obtained using image processing techniques.

5.2 Simulation Setup. Although 3D model of the insertion procedure is implemented, a 2D dynamic model is used in this section for ease of illustration and result comparison. The simulated tissue properties are obtained from the tests using the phantoms made from the same batch that will be used in the experiments, so that the simulation setup agrees with the experiments. The phantom's dimension parameters are measured directly. The Young's modulus and Poisson ratio of the phantom are tested by the compression experiments [27], and the average values are used. The area density is calculated with the measured mass and dimensions, respectively. The specific parameters in the simulation are listed in Table 1. In the experiments, the moment when the needle contacting the tissue's surface was regarded as zero time. The initial positions of the markers were regarded as their origin.

A snapshot of the simulation result is shown in Fig. 14, in which the "*" points are the target points corresponding to the same marker position in the phantom at the beginning of the experiments, as shown in Fig. 15. As it can be seen from the simulation and experiment, the direction and the distribution of the points in the simulation are similar to those in the experiment.

5.3 Results and Comparisons. Three types of tissue nodes are selected to illustrate the effectiveness of the proposed simulation model. As shown in Fig. 15, the first type is the nodes constrained by the needle, which means they are close to the needle track (target 1 and 3). The second type is the nodes close to the boundary (target 5 and 10), and the third type is the nodes that are far away from the needle (target 8 and 9).

Target 1 and target 3 are near to the needle path, so their displacements are bigger than those of other targets, as shown in Fig. 16. The simulated track of target 1 can be covered by a rectangular area with the width of 0.7 mm. The simulated track of target 3 can be covered by a rectangular area with the width of 0.35 mm. As it can be seen from this figure, the simulation trajectories agree well to the experimental results. The marker "▷" denotes simulation results, and the marker "*" denotes the experimental results. The tracks in the simulation are more consistent than that in the experiments, whose variation in each interval is small and nearly even.
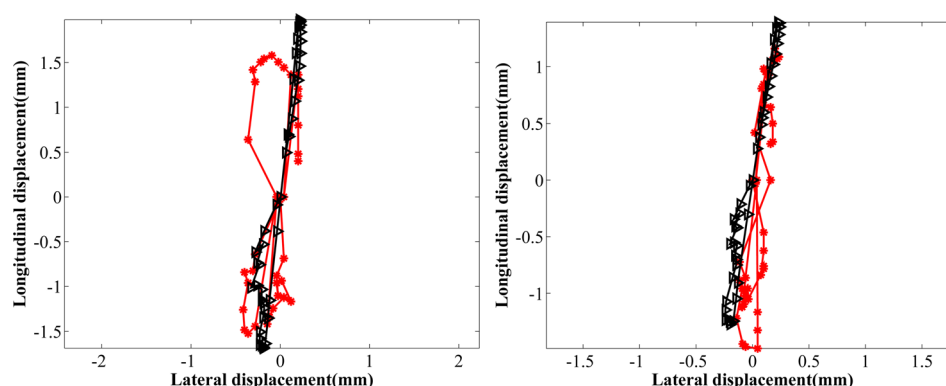

Fig. 16 The comparison of the trajectory of target 1 (left) and 3 (right), "▷" denotes the simulation results, "⋆" denotes the experimental results
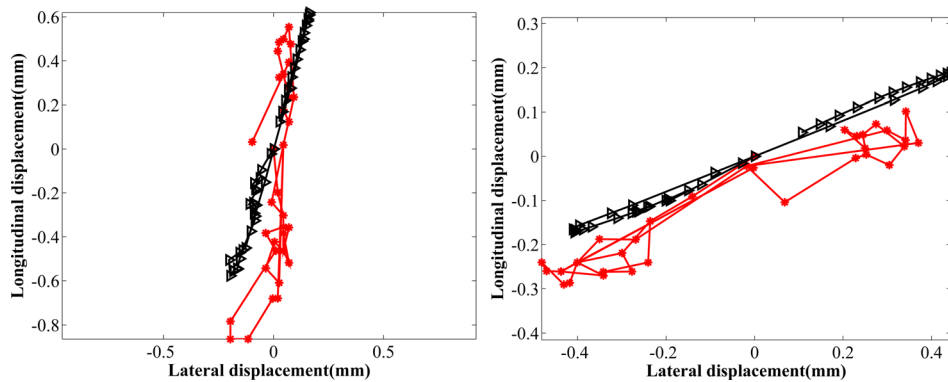
Fig. 17 The comparison of the trajectories of targets 5 (left) and 10 (right)
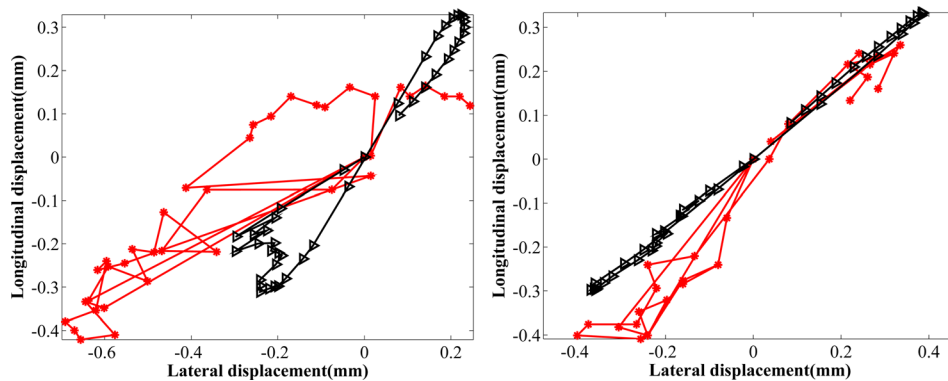

Fig. 18 The comparison of the trajectory of target 8 (left) and 9 (right)

Target 5 and target 10 are located close to the bottom of the tissue, so their longitudinal displacements in the simulation is smaller than that in experiment, as shown in Fig. 17. The simulated tracks of target 5 and 10 can be covered by two rectangular areas with the width of 0.4 mm and 0.25 mm, respectively. Targets 8 and 9 were far from the needle, so their displacements are small, as shown in Fig. 18. The simulated tracks of targets 8 and 9 can be covered by two rectangular areas with the width of 0.3 mm and 0.15 mm, respectively.

As it can be seen from the comparisons of simulated and experimental results, the simulation results agree well with the experimental results. The maximum absolute error between the simulated and experimental result is less than 0.8 mm.

6 Conclusion and Future Work

In this paper, a novel simulation algorithm is developed for needle insertion into soft tissue. The axial force of the needle is modeled as a combination of friction force and cutting force, and the radial force is modeled as the virtual spring. The needle–tissue interaction model is developed based on modified local constraint method, where the interactive forces between the needle and the tissue are balanced through the integration of needle–force and tissue–force relationships. A testbed is constructed, and the experiments are designed to obtain the model parameters and validate the proposed method using artificial phantom with markers. It is shown from the results that the simulated tissue deformations agree well with the experimental observations with sufficient accuracy. Future work needs to additionally investigate the extension of the proposed algorithm for real-time calculation of larger dimensional 3D models with inhomogeneous tissue properties. In addition, online tissue model parameter identification method need to be developed to estimate the parameters of the soft tissue model during the needle insertion procedure, which can reduce the modeling errors and improve the accuracy of needle insertion procedure.

References

[1] Abolhassani, N., 2007, "Needle Insertion Into Soft Tissue: A Survey," Med. Eng. Phys., **29**(4), 5, pp. 413–431.
[2] Gao, D., Lei, Y., and Zheng, H., 2012, "Needle Steering for Robot-Assisted Insertion Into Soft Tissue: A Survey," Chin. J. Mech. Eng., **25**(4), pp. 629–638.
[3] Nienhuys, H.-W., and van der Stappen, A. F., 2003, "Interactive Needle Insertions in 3d Nonlinear Material," Institute of Information Computing Science, Utrecht University, Utrecht, Netherlands, available at: www.cs.uu.nl.
[4] Hing, J. T., Brooks, A. D., and Desai, J. P., 2006, "Reality-Based Needle Insertion Simulation for Haptic Feedback in Prostate Brachytherapy," 2006 IEEE International Conference on Robotics and Automation, IEEE, pp. 619–624.
[5] Okamura, A. M., Simone, C., and O'Leary, M. D., 2004, "Force Modeling for Needle Insertion Into Soft Tissue," IEEE Trans. Biomed. Eng., **51**(10), pp. 1707–1716.
[6] Moore, J. Z., Malukhin, K., Shih, A. J., and Ehmann, K. F., 2011, "Hollow Needle Tissue Insertion Force Model," CIRP Ann. Manuf. Technol., **60**(1), pp. 157–160.
[7] Fukushima, Y., Saito, K., and Naemura, K., 2013, "Estimation of the Cutting Force Using the Dynamic Friction Coefficient Obtained by Reaction Force During the Needle Insertion," Proc. CIRP, **5**, pp. 265–269.
[8] Crouch, J. R., Schneider, C. M., Wainer, J., and Okamura, A. M., 2005, "A Velocity-Dependent Model for Needle Insertion in Soft Tissue," *Medical Image Computing and Computer-Assisted Intervention—Miccai 2005*, Vol. 3750. Springer, Berlin, Germany, pp. 624–632.
[9] Asadian, A., Patel, R. V., and Kermani, M. R., 2014, "Dynamics of Translational Friction in Needle-Tissue Interaction During Needle Insertion," Ann. Biomed. Eng., **42**(1), pp. 73–85.

[10] Fukushima, Y., and Naemura, K., 2014, "Estimation of the Friction Force During the Needle Insertion Using the Disturbance Observer and the Recursive Least Square," ROBOMECH J., **1**(1), pp. 1–8.

[11] Barnett, A. C., Lee, Y.-S., and Moore, J. Z., 2015, "Fracture Mechanics Model of Needle Cutting Tissue," ASME J. Manuf. Sci. Eng., **138**(1), p. 011005.

[12] Misra, S., Reed, K. B., Schafer, B. W., and Okamura, A. M., 2009, "Observations and Models for Needle-Tissue Interactions," 2009 IEEE International Conference on Robotics and Automation, IEEE, pp. 2687–2692.

[13] Roesthuis, R. J., Veen, Y. R. V., Jahya, A., and Misra, S., 2011, "Mechanics of Needle-Tissue Interaction," 2011 IEEE/RSJ International Conference on Intelligent Robots and Systems, IEEE, pp. 2558–2563.

[14] Sadjadi, H., Hashtrudi-Zaad, K., and Fichtinger, G., 2014, "Needle Deflection Estimation: Prostate Brachytherapy Phantom Experiments," ROBOMECH J., **9**(6), pp. 921–929.

[15] Dehghan, E., Goksel, O., and Salcudean, S. E., 2006, *A Comparison of Needle Bending Models*, Springer, Berlin Heidelberg, Germany.

[16] Shan, J., Pan, L., Yan, Y., Jun, L., and Zhiyong, Y., 2014, "Experimental Study of Needle-Tissue Interaction Forces: Effect of Needle Geometries, Insertion Methods and Tissue Characteristics," J. Biomech., **47**(13), pp. 3344–3353.

[17] Abolhassani, N., Patel, R., and Ayazi, F., 2007, "Effects of Different Insertion Methods on Reducing Needle Deflection," Engineering in Medicine and Biology Society, EMBS 2007, 29th Annual International Conference of the IEEE, pp. 491–494.

[18] Mahvash, M., and Dupont, P. E., 2009, "Fast Needle Insertion to Minimize Tissue Deformation and Damage," IEEE International Conference on Robotics and Automation, 2009, ICRA'09, IEEE, pp. 3097–3102.

[19] DiMaio, S. P., and Salcudean, S. E., 2003, "Needle Insertion Modeling and Simulation," IEEE Trans. Rob. Autom., **19**(5), pp. 864–875.

[20] Pezzementi, Z., Ursu, D., Misra, S., and Okamura, A. M., 2008, "Modeling Realistic Tool-Tissue Interactions With Haptic Feedback: A Learning-Based Method," 2008 Symposium on Haptic Interfaces for Virtual Environment and Teleoperator Systems, IEEE, pp. 209–215.

[21] Kobayashi, Y., Onishi, A., Hoshi, T., Kawamura, K., Hashizume, M., and Fujie, M. G., 2009, "Development and Validation of a Viscoelastic and Nonlinear Liver Model for Needle Insertion," Int. J. Comput. Assisted Radiol. Surg., **4**(1), pp. 53–63.

[22] Buijs, J. O. D., Hansen, H. H., Lopata, R. G., Korte, C. L. d., and Misra, S., 2011, "Predicting Target Displacements Using Ultrasound Elastography and Finite Element Modeling," IEEE Trans. Biomed. Eng., **58**(11), pp. 3143–3155.

[23] Goksel, O., Salcudean, S. E., Dimaio, S. P., Rohling, R., and Morris, J., 2005, *3D Needle-Tissue Interaction Simulation for Prostate Brachytherapy*, Springer, Berlin Heidelberg, Germany.

[24] Haddadi, A., and Hashtrudi-Zaad, K., 2011, "Development of a Dynamic Model for Bevel-Tip Flexible Needle Insertion Into Soft Tissues," Engineering in Medicine and Biology Society, EMBC, Annual International Conference of the IEEE, pp. 7478–7482.

[25] Alterovitz, R., Goldberg, K., and Okamura, A., 2005, "Planning for Steerable Bevel-Tip Needle Insertion Through 2d Soft Tissue With Obstacles," IEEE International Conference on Robotics and Automation, ICRA 2005, pp. 1640–1645.

[26] Chentanez, N., Alterovitz, R., Ritchie, D., Cho, L., Hauser, K. K., Goldberg, K., Shewchuk, J. R., and O'Brien, J. F., 2009, *Interactive Simulation of Surgical Needle Insertion and Steering*, Vol. 28, ACM, New York, NY.

[27] Krouskop, T. A., Wheeler, T. M., Kallel, F., Garra, B. S., and Hall, T., 1998, "Elastic Moduli of Breast and Prostate Tissues Under Compression," Ultrason. Imaging, **20**(4), pp. 260–274.